

# C<sub>2</sub>H in prestellar cores

M. Padovani<sup>1,2</sup>, C.M. Walmsley<sup>2</sup>, M. Tafalla<sup>3</sup>, D. Galli<sup>2</sup> and H.S.P. Müller<sup>4</sup>

<sup>1</sup> Università di Firenze, Dipartimento di Astronomia e Scienza dello Spazio, Largo E. Fermi 2, I-50125 Firenze, Italy

<sup>2</sup> INAF-Osservatorio Astrofisico di Arcetri, Largo E. Fermi 5, I-50125 Firenze, Italy  
e-mail: padovani@arcetri.astro.it, walmsley@arcetri.astro.it, galli@arcetri.astro.it

<sup>3</sup> Observatorio Astronómico Nacional, Alfonso XII 3, E-28014 Madrid, Spain  
e-mail: m.tafalla@oan.es

<sup>4</sup> I. Physikalisches Institut, Universität zu Köln, Zùlpicher Straße 77, 50937 Köln, Germany  
e-mail: hspm@ph1.uni-koeln.de

Received jdate / Accepted jdate

## ABSTRACT

**Aims.** We study the abundance of C<sub>2</sub>H in prestellar cores both because of its role in the chemistry and because it is a potential probe of the magnetic field. We also consider the non-LTE behaviour of the  $N=1-0$  and  $N=2-1$  transitions of C<sub>2</sub>H and improve current estimates of the spectroscopic constants of C<sub>2</sub>H.

**Methods.** We used the IRAM 30m radiotelescope to map the  $N=1-0$  and  $N=2-1$  transitions of C<sub>2</sub>H towards the prestellar cores L1498 and CB246. Towards CB246, we also mapped the 1.3 mm dust emission, the  $J=1-0$  transition of N<sub>2</sub>H<sup>+</sup> and the  $J=2-1$  transition of C<sup>18</sup>O. We used a Monte Carlo radiative transfer program to analyse the C<sub>2</sub>H observations of L1498. We derived the distribution of C<sub>2</sub>H column densities and compared with the H<sub>2</sub> column densities inferred from dust emission.

**Results.** We find that while non-LTE intensity ratios of different components of the  $N=1-0$  and  $N=2-1$  lines are present, they are of minor importance and do not impede C<sub>2</sub>H column density determinations based upon LTE analysis. Moreover, the comparison of our Monte-Carlo calculations with observations suggest that the non-LTE deviations can be qualitatively understood. For extinctions less than 20 visual magnitudes, we derive toward these two cores (assuming LTE) a relative abundance [C<sub>2</sub>H]/[H<sub>2</sub>] of  $(1.0 \pm 0.3) \times 10^{-8}$  in L1498 and  $(0.9 \pm 0.3) \times 10^{-8}$  in CB246 in reasonable agreement with our Monte-Carlo estimates. For L1498, our observations in conjunction with the Monte Carlo code imply a C<sub>2</sub>H depletion hole of radius  $9 \times 10^{16}$  cm similar to that found for other C-containing species. We briefly discuss the significance of the observed C<sub>2</sub>H abundance distribution. Finally, we used our observations to provide improved estimates for the rest frequencies of all six components of the C<sub>2</sub>H (1–0) line and seven components of C<sub>2</sub>H (2–1). Based on these results, we compute improved spectroscopic constants for C<sub>2</sub>H. We also give a brief discussion of the prospects for measuring magnetic field strengths using C<sub>2</sub>H.

**Key words.** ISM: abundances – ISM: clouds – ISM: molecules – ISM: individual objects (L1498, CB246) – radio lines: ISM – Physical data and processes: molecular data

## 1. Introduction

The ethynyl radical C<sub>2</sub>H is a crucial intermediate in the interstellar chemistry leading to long chain carbon compounds. It has a <sup>2</sup>Σ ground state giving rise to non-negligible Zeeman splitting (Bel & Leroy 1998). These facts make it of interest to explore its abundance variations in nearby prestellar cores. In particular, it seems worthwhile to test for its presence or absence in nearby cores where CO appears to be depleted (see Bergin & Tafalla 2007). In most circumstances, CO is the main reservoir of C and thus depletion of CO seems likely to cause a reduction in the formation rate of C-containing species. However, recently Hily-Blant et al. (2008) have shown that in L1544 and L183, CN appears to be present in the high density regions where CO is depleted. This suggests that in some cases, CO depletion may be “modest” in the sense that it causes the high density core nucleus to be invisible in CO isotopomers but the depletion is not sufficient to substantially change the abundances of minor C-containing species. In view of these facts, it seems reasonable to examine the behaviour of other C-containing species in cores.

C<sub>2</sub>H is also of interest because hyperfine and spin interactions cause the rotational transitions to split into as many as 11 components which can be observed simultaneously with modern

autocorrelation spectrometers. This allows for a precise examination of the deviations from LTE in individual rotational levels and eventually an evaluation of the relative importance of collisional and radiative processes. One can observe for example in the  $N=1-0$ , 3 mm, transition six components with line strengths varying by over an order of magnitude and whose relative intensities can be compared extremely precisely. Departures from LTE have long plagued column density estimates in molecular lines which are often uncertain by a factor of order 2 as a consequence. Reducing such uncertainties can only be achieved by understanding the causes of non-LTE behaviour in level populations and this requires both theoretical (calculations of collisional rates) and observational work. In this study, we attempt to delineate the problem in the case of C<sub>2</sub>H from an observational point of view.

We have chosen to study two cores with contrasting properties. L1498 is a well studied core in the Taurus complex at a distance of 140 parsec with a clear CO depletion hole. Its density structure has been studied in detail by Shirley et al. (2005) who conclude that their results are consistent with a “Bonnor-Ebert sphere” of central density  $1 - 3 \times 10^4$  cm<sup>-3</sup> and by Tafalla et al. (2004, 2006) who find a considerably higher central density of  $9 \times 10^4$  cm<sup>-3</sup>. Kirk et al. (2006) used SCUBA polarisation

measurements to infer a surprisingly low value of the magnetic field of  $10 \pm 7 \mu\text{G}$  in the plane of the sky. Aikawa et al. (2005) modelled the molecular distribution and concluded that their results were consistent with the contraction of a “near equilibrium” core. There is in general evidence for depletion of C-bearing species such as *c*-C<sub>3</sub>H<sub>2</sub> and C<sub>2</sub>S in a central hole of radius  $10^{17}$  cm (Tafalla et al. 2006). This is in contrast to NH<sub>3</sub> and N<sub>2</sub>H<sup>+</sup> which show no signs of depletion in the central high density region of the core.

CB246 (L1253) is a relatively isolated globule without an associated IRAS source at a distance of 140–300 parsec (Dame et al. 1987, Launhardt & Henning 1997) in the general direction of the Cepheus flare. For the purpose of this study, we adopt a distance of 200 pc. CB246 is apparently a double core seen both in NH<sub>3</sub> and C<sub>2</sub>S (Lemme et al. 1996, Codella & Scappini 1998) on a size scale of roughly 0.1 parsec. The mass (dependent on the distance) is in the range  $0.2\text{--}1 M_{\odot}$  (Codella & Scappini 1998) from the NH<sub>3</sub> maps, though there is considerable uncertainty in this. From a chemical point of view, it is interesting that there is rough general agreement between the spatial distributions seen in NH<sub>3</sub> and C<sub>2</sub>S. One aim of the present observations has been to check if C<sub>2</sub>H shows signs of depletion towards the peak emission seen in NH<sub>3</sub>.

In this article, we present IRAM 30m maps of the emission in the  $N=1\text{--}0$  transition of C<sub>2</sub>H towards CB246 and L1498. We supplement this with measurements at selected positions of the  $N=2\text{--}1$  transition of C<sub>2</sub>H as well as maps of the 1.3 mm dust emission, the  $J=1\text{--}0$  transition of N<sub>2</sub>H<sup>+</sup> and the  $J=2\text{--}1$  transition of C<sup>18</sup>O towards CB246. In Section 2, we describe our observational and data reduction procedures and in Section 3, we summarise the observational results from the line measurements. In Section 4, we attempt to use our astronomical observations to estimate rest frequencies for the individual components of C<sub>2</sub>H(1–0) and (2–1) and an updated set of hyperfine parameters. In Section 5, we give our conclusions concerning the deviations from LTE populations for C<sub>2</sub>H as well as a very tentative interpretation. In Section 6, we give our column density and abundance estimates in the two objects and discuss the evidence for depletion of C<sub>2</sub>H. In Section 7, we discuss our results and in Section 8, we summarise our conclusions.

## 2. Observations

### 2.1. C<sub>2</sub>H in L1498 and CB246

The observations were carried out with the IRAM 30m telescope. The C<sub>2</sub>H(1–0) multiplet (at 87 GHz: see Table 4) was observed at different epochs between August 2007 (only component 2, 3, 4 and 5) and July 2008 (all the components), with 1–2 mm precipitable water vapor (pwv). Observations of the C<sub>2</sub>H(2–1) multiplet (at 174 GHz: see Table 5) were performed in July 2008 with 3–4 mm pwv. The HPBW at the C<sub>2</sub>H(1–0) and C<sub>2</sub>H(2–1) frequencies are  $28''$  and  $14''$ , respectively. In August 2007, the VESPA autocorrelator was used to obtain 10 kHz channel spacing (corresponding to about  $0.034 \text{ km s}^{-1}$ ) with 20 and 40 MHz bandwidths, while in July 2008, the autocorrelator was used to obtain 20 kHz channel spacing with 20 and 40 MHz bandwidths for C<sub>2</sub>H(1–0) and 40 kHz channel spacing with 40 and 80 MHz bandwidths for C<sub>2</sub>H(2–1). In this way we covered the six hyperfine structure (HFS) components of C<sub>2</sub>H(1–0) and seven HFS components of C<sub>2</sub>H(2–1).

The two cores, L1498 and CB246, were mapped in C<sub>2</sub>H(1–0) in 2008 in raster mode with a spacing of  $20''$  (channel spacing 20 kHz) for L1498 and of  $15''$  for CB246 (thus close

to Nyquist sampling for CB246). In 2008, we also observed the C<sub>2</sub>H(2–1) line at the positions given in Table 2. Finally in 2007, we observed the C<sub>2</sub>H(1–0) line towards the (0,0) offset with 10 kHz resolution in both sources.

The observed strategy was identical for all measurements: frequency-switching mode with a 7.5 MHz throw and a phase time of 0.5 s, with a calibration every 10 to 15 minutes. The data were reduced using CLASS, the line data analysis program of the GILDAS software<sup>1</sup>. Instrumental bandpass and atmospheric contributions were subtracted with polynomial baselines, before and after the folding of the two-phase spectra. The final rms, in the main-beam temperature ( $T_{\text{mb}}$ ), in each channel of width  $\delta\nu = 0.067 \text{ km s}^{-1}$  is  $\sigma_T \sim 50 \text{ mK}$  for both L1498 and CB246 and for both the  $N=1\text{--}0$  and the  $N=2\text{--}1$  transitions, while the system temperatures are  $T_{\text{sys}} \sim 130 \text{ K}$  for the  $N=1\text{--}0$  transition and  $T_{\text{sys}} \sim 1000 \text{ K}$  for the  $N=2\text{--}1$  transition. In what follows, all temperatures are on the main-beam scale,  $T_{\text{mb}} = F_{\text{eff}} T_{\text{A}}^* / B_{\text{eff}}$ , where  $T_{\text{A}}^*$  is the antenna temperature corrected for atmospheric absorption, and the forward and beam efficiencies are respectively  $F_{\text{eff}} = 0.95$  and  $B_{\text{eff}} = 0.77$  concerning the  $N=1\text{--}0$  transition and  $F_{\text{eff}} = 0.93$  and  $B_{\text{eff}} = 0.65$  for the  $N=2\text{--}1$  transition.

### 2.2. N<sub>2</sub>H<sup>+</sup>(1–0) and C<sup>18</sup>O(2–1) in CB246

Observations of the N<sub>2</sub>H<sup>+</sup>(1–0) multiplet (at 93 GHz) and C<sup>18</sup>O(2–1) (at 219 GHz) in CB246 were carried out simultaneously in July 2008, with 3–4 mm pwv. The HPBW at the N<sub>2</sub>H<sup>+</sup>(1–0) and C<sup>18</sup>O(2–1) frequencies are  $26''$  and  $11''$  respectively. The VESPA autocorrelator was used to obtain 10 kHz channel spacing with 40 MHz bandwidth for N<sub>2</sub>H<sup>+</sup>(1–0) and 20 kHz channel spacing with 40 MHz bandwidth for C<sup>18</sup>O(2–1). We observed using the frequency-switching mode with a 7.5 MHz throw for N<sub>2</sub>H<sup>+</sup>(1–0) and a 15 MHz throw for C<sup>18</sup>O(2–1) and a phase time of 0.5 s with a calibration every 10 to 15 minutes. We observed a region of 2.5 arc minutes squared in extent with a spacing of  $15''$ . Thus, the N<sub>2</sub>H<sup>+</sup> map is essentially Nyquist sampled whereas C<sup>18</sup>O is under-sampled (though the maps shown subsequently are smoothed to a resolution of  $26''$ ).

For N<sub>2</sub>H<sup>+</sup>, the final rms, in main-beam temperature units ( $T_{\text{mb}}$ ), in channels of width  $\delta\nu = 0.031 \text{ km s}^{-1}$  was  $\sigma_T \sim 110 \text{ mK}$ , with a  $T_{\text{sys}} \sim 160 \text{ K}$ . For C<sup>18</sup>O, the final rms (channels of width  $\delta\nu = 0.027 \text{ km s}^{-1}$ ) was  $\sigma_T \sim 200 \text{ mK}$ , with a  $T_{\text{sys}} \sim 400 \text{ K}$ . The forward and the beam efficiencies are respectively  $F_{\text{eff}} = 0.95$  and  $B_{\text{eff}} = 0.77$  for N<sub>2</sub>H<sup>+</sup> and  $F_{\text{eff}} = 0.91$  and  $B_{\text{eff}} = 0.55$  for C<sup>18</sup>O.

### 2.3. Bolometer map of CB246

CB246 was observed in the 1.3 mm continuum with the IRAM 30m telescope in May, November and December 2007. We used the MAMBO2 117-channel bolometer array in the on-the-fly mode with a scanning speed of  $6'' \text{ s}^{-1}$ , a wobbler period of 0.5 s and a wobbler throw of  $70''$ , reaching an rms of 3 mJy/beam. The bolometer central frequency is 250 GHz and the half power bandwidth (HPBW) at 1.3 mm is approximately  $11''$ .

## 3. Observational results

### 3.1. C<sub>2</sub>H(1–0)

In Fig. 1, we show our map of the integrated intensity in the C<sub>2</sub>H(1–0) ( $J', F' \rightarrow J, F = 3/2, 2 \rightarrow 1/2, 1$ ) transition su-

<sup>1</sup> <http://www.iram.fr/IRAMFR/GILDAS>.

perposed on the map of the 1.3 mm dust continuum emission smoothed at 28'' together with the positions observed in the  $N=2-1$  transition. One sees that towards L1498, while the dust emission has a single peak at the centre of the map, the C<sub>2</sub>H emission has a broad “plateau” with an extent rather similar to that of the dust, showing two peaks to the SE and NW of the dust emission peak. Rather similar distributions have been seen in several other C-bearing species (e.g. CS, C<sub>2</sub>S, CO and  $c$ -C<sub>3</sub>H<sub>2</sub>, see Tafalla et al. 2002 and Tafalla et al. 2006) and has been attributed to depletion onto grain surfaces in the dense gas associated with the dust continuum peak. Our data suggest that C<sub>2</sub>H behaves in a similar fashion towards L1498.

The situation is rather different towards CB246 (see Fig. 2, upper panel) where we see that the dust and C<sub>2</sub>H emission have rather similar distributions. Both are double peaked, although the C<sub>2</sub>H NW emission peak is offset about 30'' to the south of its counterpart in dust emission whereas towards the SE peak the difference is marginal.

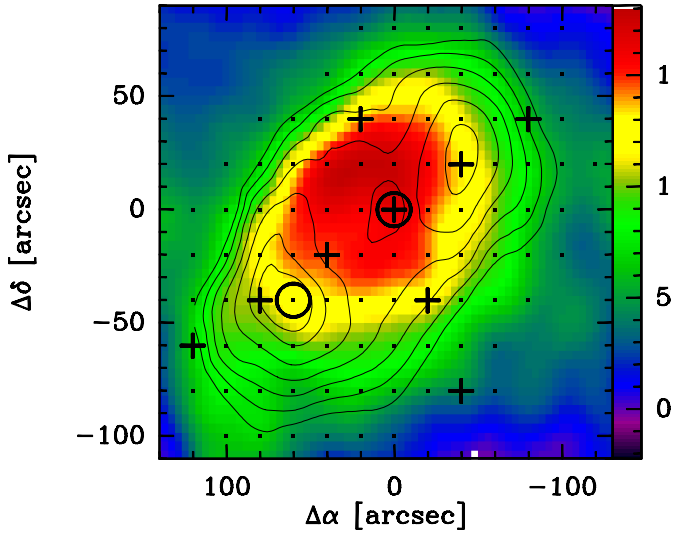


Fig. 1: Dust emission at 1.3 mm (after smoothing to 28'', *coloured map*) towards L1498, from Tafalla et al. (2002), superposed to the emission of C<sub>2</sub>H(1–0) ( $J', F' \rightarrow J, F = 3/2, 2 \rightarrow 1/2, 1$ ), *black contours*. Contours represent 40, 50, 60, 70, 80, 90 and 95 per cent of the peak value which is 0.67 K km s<sup>−1</sup>. The scale bar to the right of each panel gives the continuum flux in mJy/beam. The *crosses* indicate the positions used for the cuts in Fig. 3 while the *circles* show positions observed in C<sub>2</sub>H(2–1). The (0,0) position corresponds to  $\alpha(2000) = 04^{\text{h}}10^{\text{m}}51.5^{\text{s}}$ ,  $\delta(2000) = 25^{\circ}09'58''$ .

It is interesting to compare the distributions of different components. We do this in Fig. 3 where we compare cuts in all the 1–0 component lines with cuts in the continuum intensity. One sees that ratios of different pairs of components do not vary greatly along these cuts, although the ratio of the strong 87316 MHz component (no. 2 in Table 4) to the weak 87284 MHz line (no. 1) at the L1498 dust peak is somewhat smaller (about 45%) than elsewhere in the cut. However, this ratio is always of order 3 as compared to the expected value of 10 for optically thin emission (suggesting a moderately optically thick 87316 MHz line). There are thus indications of saturation of the stronger components of the C<sub>2</sub>H(1–0) line and we conclude that optical depth effects are present but lines have moderate opacities, as shown in Table 1 for selected positions in the two observed sources. It is

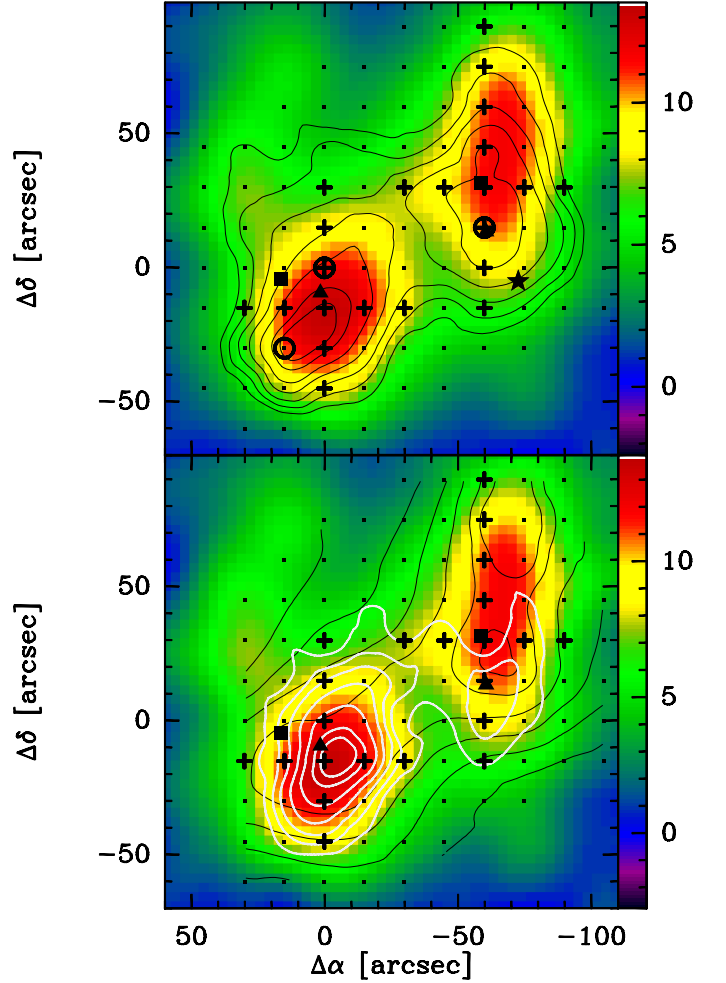


Fig. 2: Upper panel: dust emission at 1.3 mm (after smoothing to 28'', *coloured map*) towards CB246 (see Sect. 2.3), superposed to the emission of C<sub>2</sub>H(1–0) ( $J', F' \rightarrow J, F = 3/2, 2 \rightarrow 1/2, 1$ ); *circles* show positions observed in C<sub>2</sub>H(2–1); *asterisk* shows the position of the 2MASS object (see Sect. 3.4). Lower panel: dust emission at 1.3 mm (after smoothing to 26'', *coloured map*) towards CB246 superposed to the emission of C<sup>18</sup>O(2–1), *black contours*, and N<sub>2</sub>H<sup>+</sup>(1–0) ( $F'_1, F' \rightarrow F_1, F = 1, 2 \rightarrow 0, 1$ ), *white contours*; Both panel: contours represent 40, 50, 60, 70, 80, 90 and 95 per cent of the peak values which are 0.67, 0.70 and 0.39 K km s<sup>−1</sup> for C<sub>2</sub>H(1–0), C<sup>18</sup>O(2–1) and N<sub>2</sub>H<sup>+</sup>(1–0), respectively; the crosses indicate the positions used for the cuts in Fig. 3 and 6; *solid triangles* represent the peaks of NH<sub>3</sub>(1,1), from Lemme et al. (1996), and *solid squares* the peaks of C<sub>2</sub>S(2<sub>1</sub>–1<sub>0</sub>), from Codella & Scappini (1998). The scale bar to the right of each panel gives the continuum flux in mJy/beam. The (0,0) position corresponds to  $\alpha(2000) = 23^{\text{h}}56^{\text{m}}43.6^{\text{s}}$ ,  $\delta(2000) = 58^{\circ}34'09''$ .

noticeable also that while C<sub>2</sub>H has a minimum towards the dust peak in L1498 (and we conclude this is a real column density minimum), there is a little indication of variation in the ratio of C<sub>2</sub>H to dust continuum intensity crossing the SE peak in CB246.

Another indication of line transfer effects can be obtained from comparing line profiles of the different C<sub>2</sub>H(1–0) components as shown in Fig. 4 where we show the high (10 kHz) spectral resolution data from 2007. It is noticeable that towards the dust peak, the weakest 87407 MHz component (no. 5 in Table 4) has a maximum at a velocity where the strong 87316 MHz

Table 1: Line parameters<sup>a</sup> observed in C<sub>2</sub>H(1–0)

$\alpha, \delta$ offsets ["", ""]	$V_{\text{LSR}}$ [km s <sup>-1</sup> ]	$\Delta V$ [km s <sup>-1</sup> ]	$\tau_{\text{total}}^b$
L1498			
0, 0	7.80(0.01)	0.17(0.01)	29.4(0.3)
60, -40	7.74(0.03)	0.21(0.01)	28.3(0.4)
CB246			
0, 0	-0.83(0.01)	0.24(0.01)	13.5(0.3)
15, -30	-0.78(0.01)	0.26(0.01)	20.9(1.1)
-60, 15	-0.87(0.01)	0.27(0.01)	14.4(0.7)

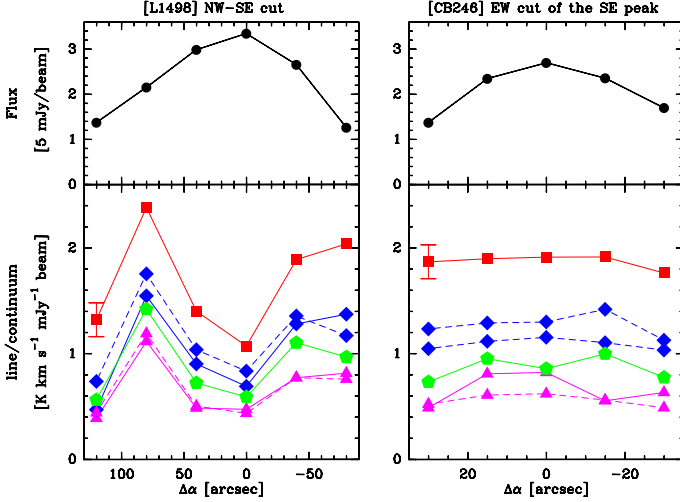
<sup>a</sup> Numbers in parentheses represent the errors from the fit.<sup>b</sup> Sum of the peak optical depth of the six hyperfine components.

Fig. 3: Upper panels: Continuum emission flux measured along the NW-SE cut in L1498, see Fig. 1, and along the EW cut of the SE peak in CB246, see upper panel of Fig. 2. Lower panels: ratio between the integrated intensity of the different hyperfine components of C<sub>2</sub>H(1–0) with the continuum emission flux in the same positions of the upper panels. The typical error on the ratio is 0.16 K km s<sup>-1</sup> mJy<sup>-1</sup> beam (component 1, *solid magenta line with triangles*; component 2, *solid red line with squares*; component 3, *solid blue line with diamonds*; component 4, *dashed blue line with diamonds*; component 5, *solid green line with pentagons*; component 6, *dashed magenta line with triangles*; component labels are given in Table 4).

line (no. 2) shows a dip between two peaks. This is the signature expected for “self-absorption” by a foreground layer of density lower than that responsible for the bulk of the emission. The effect however is not sufficiently strong to change the above conclusions concerning the importance of optical depth effects. We note moreover that towards CB246, no effects of this type are seen.

### 3.2. C<sub>2</sub>H(2–1)

The C<sub>2</sub>H(2–1) line has had little (if any) attention and it was thus interesting that we succeeded in detecting 7 of the 11 components of the line in both sources. Line parameters are given in Table 2 and sample profiles are shown in Fig. 5. It is interesting (see discussion below) that within the errors, line intensities are consistent with LTE but that, in particular towards L1498, the total optical depth derived from an LTE fit (see Table 2) is large and corresponds to an optical depth of 3.1 in the strongest

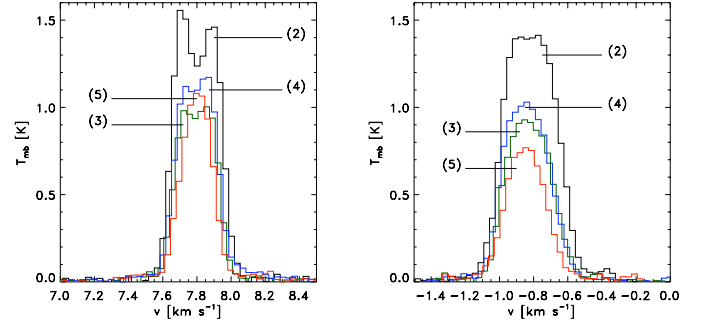


Fig. 4: Component 2 (*black*), 3 (*green*), 4 (*blue*) and 5 (*red*) of C<sub>2</sub>H(1–0) observed at high resolution in 2007 at the offset (0,0) in L1498 (left panel) and CB246 (right panel). In order to compare line shapes and intensities, components have been shifted in frequency. Component labels and rest frequencies are given in column 1 and 3 of Table 4).

174663 MHz component (no. 2 of Table 5). We note however that slight errors in rest frequencies could influence this interpretation.

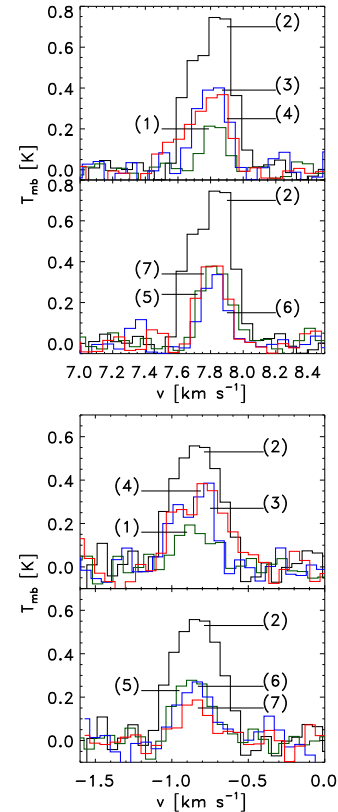


Fig. 5: Hyperfine components of C<sub>2</sub>H(2–1) observed at the offset (0,0) in L1498 (left panel) and CB246 (right panel). In order to compare line shapes and intensities, components have been shifted in frequency. Component labels and rest frequencies are given in column 1 and 3 of Table 5).

Table 2: Line parameters<sup>a</sup> observed in C<sub>2</sub>H(2–1)

$\alpha, \delta$ offsets ["", ""]	$V_{\text{LSR}}$ [km s <sup>-1</sup> ]	$\Delta V$ [km s <sup>-1</sup> ]	$\tau_{\text{total}}^b$
L1498			
0, 0	7.84(0.01)	0.23(0.01)	8.6(1.8)
60, -40	7.76(0.01)	0.25(0.01)	9.7(1.9)
CB246			
0, 0	-0.84(0.01)	0.35(0.02)	1.5(1.2)
15, -30	-0.73(0.01)	0.30(0.01)	5.4(1.0)
-60, 15	-0.88(0.01)	0.30(0.01)	5.5(1.2)

<sup>a</sup> Numbers in parentheses represent the errors from the fit.<sup>b</sup> Sum of the peak optical depth of the seven hyperfine components.

### 3.3. C<sup>18</sup>O and N<sub>2</sub>H<sup>+</sup>

In the lower panel of Fig. 2, we show a superposition of our 1.3 mm continuum map (smoothed to an angular resolution of 26'') with the C<sup>18</sup>O(2–1) and the isolated component of N<sub>2</sub>H<sup>+</sup>(1–0) ( $F'_1, F' \rightarrow F_1, F = 0, 1 \rightarrow 1, 2$ ) integrated intensity maps, together with the emission peaks in NH<sub>3</sub>(1,1), using the data obtained by Lemme et al. (1996) and in C<sub>2</sub>S(2<sub>1</sub> – 1<sub>0</sub>) by Codella & Scappini (1998). There is a general similarity between the distributions of C<sup>18</sup>O seen here and that of C<sub>2</sub>H (Fig. 2, upper panel). In general, also the C<sup>18</sup>O distribution resembles that seen in the continuum but there are clear shifts (for example in the SE) between the peaks seen in the dust emission and in C<sup>18</sup>O. In the NW, also the “bar”-like structure seen in the continuum to be extended N-S is also present in C<sup>18</sup>O but seems even more elongated (dimensions of 100'' in the continuum as compared to 120'' in C<sup>18</sup>O).

To the SE there is reasonable agreement between the continuum and N<sub>2</sub>H<sup>+</sup> intensity distributions and the ammonia peak appears to be consistent with these. To the NW on the other hand, the continuum is extended in a “bar”-like feature and N<sub>2</sub>H<sup>+</sup> (but also C<sub>2</sub>H) peaks at the south end of this 40'' to the south of the continuum peak. These differences suggest chemical differentiation in CB246 albeit on a scale smaller than in L1498. Besides, the N<sub>2</sub>H<sup>+</sup> peaks resemble the continuum structure in the SE but differ considerably in the NW suggesting that in this case (in contrast to L1498 and L1544, see Tafalla et al. 2006), the N<sub>2</sub>H<sup>+</sup> abundance may be varying with position. The shift between the N<sub>2</sub>H<sup>+</sup> NW peak and the continuum peak is unusual, but not unprecedented (see Pagani et al. 2007). However, a more detailed study of the radiative transfer and excitation is needed to confirm this.

In Fig. 6 we compare cuts in the strongest component of C<sub>2</sub>H(1–0) (component 2, see Table 4), C<sup>18</sup>O(2–1) and the isolated component of N<sub>2</sub>H<sup>+</sup>(1–0) with cuts in the continuum intensity. N<sub>2</sub>H<sup>+</sup> and C<sup>18</sup>O show a rather constant line-to-continuum ratio in the SE peak cut, while in the NW peak cut, these molecules do not look like the continuum structure, especially the C<sup>18</sup>O emission which appears to be shifted down compared to the continuum emission.

### 3.4. Mass of CB246

In the continuum, CB246 shows a double-peaked profile, with a rounded SE clump with a radius (measured at half-power contour) of 33'' (corresponding to 0.03 pc at the distance of 200 pc) and a more elliptical NW clump with a major and a minor axes of 100'' (or 0.1 pc) and 44'' (or 0.04 pc), respectively. Dust emission is generally optically thin at millimetre wavelengths and hence is a direct tracer of the mass content of molecular cloud cores.

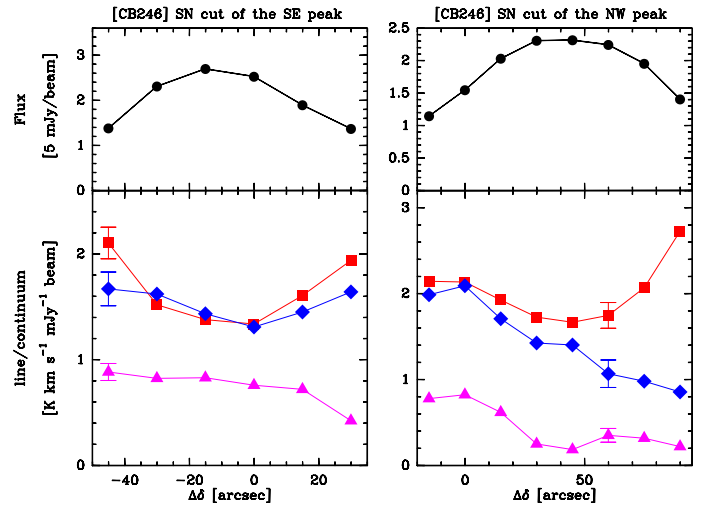


Fig. 6: Upper panels: Continuum emission flux measured along the SN cut of the SE and the NW peaks in CB246, see upper panel of Fig. 2. Lower panels: ratio between the integrated intensity of the component 2 of C<sub>2</sub>H(1–0), red squares, C<sup>18</sup>O(2–1), blue diamonds, and the isolated component of N<sub>2</sub>H<sup>+</sup>(1–0), magenta triangles, with the continuum emission flux in the same positions of the upper panels. The typical errors on the ratio are 0.16, 0.15 and 0.08 K km s<sup>-1</sup> mJy<sup>-1</sup> beam for C<sub>2</sub>H, C<sup>18</sup>O and N<sub>2</sub>H<sup>+</sup> respectively.

In the hypothesis of an isothermal dust source, the total (dust plus gas) mass is related to the millimetre flux density,  $S_{1.3}$ , integrated over the solid angle  $\Omega_{\text{beam}}$  according to the following equation

$$M = \frac{S_{1.3} d^2}{\kappa_{1.3} B_{1.3}(T_d)} \quad (1)$$

where  $B_{1.3}(T_d)$  is the Planck function calculated at the dust temperature  $T_d = 10$  K and  $\kappa_{1.3}$  is the dust opacity per unit mass which is assumed constant and equal to 0.005 cm<sup>2</sup> g<sup>-1</sup> for prestellar cores of intermediate densities ( $n \lesssim 10^5$  cm<sup>-3</sup>), assuming a gas-to-dust mass ratio of 100 (Henning et al. 1995, Preibisch et al. 1993). We found a FWHM of 1.2 M<sub>⊙</sub> for both clumps and a total mass of 3.3 M<sub>⊙</sub> which has been evaluated taking into account the continuum flux above two times the rms. The average column and number density of molecular hydrogen have been evaluated within the same area used to compute the mass and are to  $N(\text{H}_2) = 1.9 \times 10^{22}$  cm<sup>-2</sup> and  $n(\text{H}_2) = 7.6 \times 10^4$  cm<sup>-3</sup>, respectively.

To the south of the NW emission peak, there is a bright infrared source (2MASS J23563433+5834043, see Fig. 2) which appears to be a heavily reddened background star with visual extinction of  $\sim 20$  magnitudes, consistent with our column density estimates.

### 3.5. Gas kinematics

From the hyperfine fit of C<sub>2</sub>H(1–0), using the rest frequencies discussed below (see Sect. 4.1), we derived the line center velocities,  $V_{\text{LSR}}$ , and in Fig. 7 we present the radial profiles which are almost flat on the average, especially for L1498. Radii are computed with respect to the offset (0,0) for the two sources (see Fig. 1 and 2).

Following Goodman et al. (1993), we checked for the presence of a velocity gradient,  $\mathcal{G}$ , across these two cores using



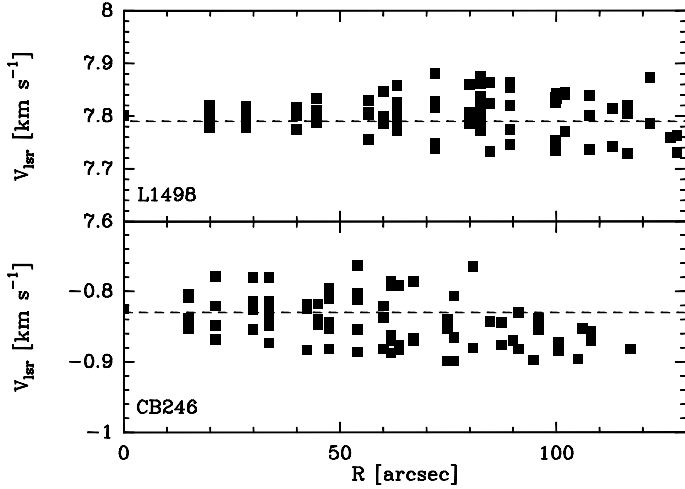


Fig. 7: Radial profile of line center velocity for L1498 (upper panel) and CB246 (lower panel) derived from the hyperfine-structure fits of C<sub>2</sub>H(1–0). The uncertainty of the velocity estimates is of the order of 0.003 km s<sup>−1</sup> and the dashed line represents the mean value.

C<sub>2</sub>H(1–0) data. A further check has been done on CB246 using N<sub>2</sub>H<sup>+</sup>(1–0) and C<sup>18</sup>O(2–1) data, finding a good agreement within the errors with the corresponding values from C<sub>2</sub>H. In Fig. 8 we show the local velocity gradients in the two cores and in Table 3 we show our results as regards the velocity gradient,  $\mathcal{G}$ , its direction,  $\Theta_{\mathcal{G}}$  and the mean LSR velocity,  $\langle V_{\text{LSR}} \rangle$ . All these quantities are in good agreement with the estimates of Goodman et al. (1993) and Tafalla et al. (2004) who observed L1498 using NH<sub>3</sub> and N<sub>2</sub>H<sup>+</sup> as a tracer. Besides, we evaluated the angular velocity,  $\omega$ , assuming that the angular velocity vector points in the direction given by  $\hat{\omega}$ , that is  $\omega = (\mathcal{G} / \sin i) \hat{\omega}$ , where  $i$  is the inclination of  $\omega$  to the line of sight and the position angle of  $\hat{\omega}$  is given by  $\Theta_{\hat{\omega}} = \Theta_{\mathcal{G}} + \pi/2$ . Statistically, for a random distribution of orientation,  $\langle \sin i \rangle^{-1} = 4/\pi$  (Chandrasekhar & Münch 1950, Tassoul 1978). To quantify the dynamic role of the rotation in a cloud, we calculated the ratio between the rotational and the gravitational energy, denoted with  $\beta$ . For a uniform density sphere,  $\beta = (\omega^2 R^3)/(3GM)$ , where  $R$  is the rotation radius,  $G$  the gravitational constant and  $M$  the mass, and the specific angular momentum is defined as  $L/M = (2/5)R^2\omega$ .

The values of  $\beta$  we found suggest that the clouds have little rotational energy as generally found in molecular cloud cores (e.g. Goodman et al. 1993). The specific angular momentum we evaluated for these two cores is of order 10<sup>−3</sup> km s<sup>−1</sup> pc. In the hypothesis that a core has been formed from a parental clump with equal mass and at the same galactocentric distance of the core (about 7 kpc for L1498 and CB246), we computed a rotation frequency of order 10<sup>−15</sup> s<sup>−1</sup> assuming that the angular momentum of the clump is due to Galactic differential rotation (Clemens, 1985). This value corresponds to a specific angular momentum of 3 × 10<sup>−2</sup> km s<sup>−1</sup> pc, that is 30 times greater than the  $L/M$  of the cores. This shows that the specific angular momentum of the cores is low compared to larger (galactic) scales. Thus angular momentum is lost in forming cores as expected by Ohashi (1999) for cores with radius greater than 0.03 pc. In particular, the cores lie on the relation founded by Ohashi (1999) for  $L/M$  as a function of the radius.

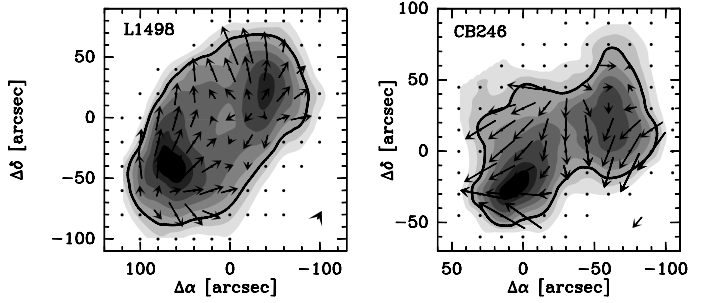


Fig. 8: C<sub>2</sub>H(1–0) velocity gradient toward L1498 (upper panel) and CB246 (lower panel): the integrated intensity map of component 2 of C<sub>2</sub>H is shown in gray scale (black contour represents the 50% of the peak value) while arrows represent the local velocity gradients in the adjacent nine points pointing in the direction of increasing velocity and with the length proportional to the magnitude. The arrow in the bottom-right corner represents the total velocity gradient.

Table 3: Results of gradient fitting.

quantity	unit	L1498	CB246
$\mathcal{G}$	[km s <sup>−1</sup> pc <sup>−1</sup> ]	0.56 ± 0.05	0.65 ± 0.09
$\Theta_{\mathcal{G}}$	[deg E of N]	−37 ± 1	143 ± 4
$\langle V_{\text{LSR}} \rangle$	[km s <sup>−1</sup> ]	7.79 ± 0.04	−0.83 ± 0.05
$\omega$	[10 <sup>−14</sup> s <sup>−1</sup> ]	2.3 ± 0.2	2.7 ± 0.4
$\beta$	[10 <sup>−3</sup> ]	~ 2.5	~ 4.0
$L/M$	[10 <sup>−3</sup> km s <sup>−1</sup> pc]	1.0 ± 0.2	1.2 ± 0.4

#### 4. Evaluation of new spectroscopic parameters for C<sub>2</sub>H

The C<sub>2</sub>H radical is a linear molecule. Its unpaired electron causes a splitting of each rotational level into two fine structure levels. In addition, the spin of the H nucleus causes each fine structure level to be split further into two hyperfine levels. The strong transitions are those having  $\Delta N = \Delta J = \Delta F$  which leads to four strong transitions at higher quantum numbers. However, transitions with  $\Delta N \neq \Delta J$  or with  $\Delta J \neq \Delta F$ , which have essentially vanishing intensities at high  $N$ , may have fairly large relative intensities at lower values of  $N$ ; the only restriction which has to be followed strictly is  $\Delta F = 0$  or  $\pm 1$ . In the case of the  $N=1-0$  and  $N=2-1$  transitions, this leads to 6 and 11 hyperfine lines, respectively, with non-zero intensity.

##### 4.1. Rest frequencies

Previous rotational data of C<sub>2</sub>H have been summarised by Müller et al. (2000). They had measured submillimetre transitions up to 1 THz; the small hydrogen hyperfine splitting was not resolved. Their data set also included 6 hyperfine lines of the  $N=1-0$  measured toward a position north of Orion-KL (Gottlieb et al. 1983), four hyperfine components of the  $N=2-1$  transition obtained in the laboratory by the same authors as well as four  $N=3-2$  hyperfine features (Sastry et al. 1981). These data as well as predictions are available from the recommended CDMS<sup>2</sup> (Cologne Database for Molecular Spectroscopy, Müller et al. 2001, 2005).

<sup>2</sup> <http://www.astro.uni-koeln.de/cdms/>

In the present investigation we have observed all six HFS components of the  $N=1-0$  transition as well as seven components of the  $N=2-1$  transition. Because of good to very good signal-to-noise (S/N) ratios of all these lines and because of the small line width it seemed promising to determine improved rest frequencies for these lines with respect to those available in the CDMS. The main sources affecting the accuracy of rest frequencies, besides S/N and line width are expected to be the symmetry of the (usually Gaussian) line shapes and the accuracy with which the velocity structure of the source is known. On the basis of the well determined rest frequencies of N<sub>2</sub>H<sup>+</sup>(1–0) (Pagani et al. 2009) and C<sup>18</sup>O(2–1) (Müller et al. 2001) we have derived at the dust continuum peak an LSR velocity of 7.80 km s<sup>−1</sup> for L1498 based on the observations of these two transitions by Tafalla et al. (2002) and an LSR velocity of −0.83 km s<sup>−1</sup> for CB246 from the present observations of these transitions (see Sect. 2.2). Employing these LSR velocities, rest frequencies of C<sub>2</sub>H have been determined separately for the two observed sources. They differ on average by 3 and 17 kHz, respectively, for the  $N=1-0$  and  $N=2-1$  transition and the averages for each HFS component are given in Table 4 and 5, respectively together with the assignments, the estimated uncertainties, the residuals o–c between the observed frequencies and those calculated from the final set of spectroscopic parameters, and the relative intensities  $f$ .

Table 4: Observed hyperfine structure components of the  $N' \rightarrow N = 1 \rightarrow 0$  transition in C<sub>2</sub>H: rest frequencies<sup>a</sup>, residuals o–c between observed and calculated frequencies<sup>b</sup>, and relative intensities  $f$ .

comp. no.	Transition $J', F' \rightarrow J, F$	$\nu$ [MHz]	o–c [kHz]	$f$
1	3/2, 1 $\rightarrow$ 1/2, 1	87284.105 (10)	−3	0.042
2	3/2, 2 $\rightarrow$ 1/2, 1	87316.898 (10)	4	0.416
3	3/2, 1 $\rightarrow$ 1/2, 0	87328.585 (10)	−2	0.207
4	1/2, 1 $\rightarrow$ 1/2, 1	87401.989 (10)	−3	0.208
5	1/2, 0 $\rightarrow$ 1/2, 1	87407.165 (10)	8	0.084
6	1/2, 1 $\rightarrow$ 1/2, 0	87446.470 (10)	0	0.043

<sup>a</sup> Numbers in parentheses are one standard deviation in units of the least significant figures.

<sup>b</sup> Calculated from present set of spectroscopic parameters in Table 6.

Table 5: Observed hyperfine structure components of the  $N' \rightarrow N = 2 \rightarrow 1$  transition in C<sub>2</sub>H: rest frequencies<sup>a</sup>, residuals o–c between observed and calculated frequencies<sup>b</sup>, and relative intensities  $f$ .

comp. no.	Transition $J', F' \rightarrow J, F$	$\nu$ [MHz]	o–c [kHz]	$f$
1	5/2, 2 $\rightarrow$ 3/2, 2	174634.861 (16)	6	0.017
2	5/2, 3 $\rightarrow$ 3/2, 2	174663.199 (12)	0	0.350
3	5/2, 2 $\rightarrow$ 3/2, 1	174667.629 (14)	−12	0.232
4	3/2, 2 $\rightarrow$ 1/2, 1	174721.744 (14)	−8	0.197
5	3/2, 1 $\rightarrow$ 1/2, 0	174728.071 (12)	12	0.083
6	3/2, 1 $\rightarrow$ 1/2, 1	174733.210 (14)	−15	0.052
7	3/2, 2 $\rightarrow$ 3/2, 2	174806.843 (14)	−7	0.045

<sup>a</sup> Numbers in parentheses are one standard deviation in units of the least significant figures.

<sup>b</sup> Calculated from present set of spectroscopic parameters in Table 6.

#### 4.2. Spectroscopic parameters

These rest frequencies, together with previous laboratory values (Sastry et al. 1981; Müller et al. 2000), were used to calculate spectroscopic parameters for C<sub>2</sub>H. As in Müller et al. (2000), the rotational constant  $B$ , the quartic and sextic distortion terms  $D$  and  $H$ , the electron spin-rotation parameter  $\gamma$  along with its distortion correction  $\gamma^D$ , as well as the scalar and tensorial electron spin-nuclear spin coupling terms  $b_F$  and  $c$  were determined. The distortion correction  $b_F^D$  to  $b_F$  was not determined with significance, even though its absolute uncertainty was slightly smaller than in Müller et al. (2000), and it did not contribute significantly to the reduction of the rms error. It was thus omitted from the final fit. However, it was found that the <sup>1</sup>H nuclear spin-rotation constant  $C$  improved the quality of the fit by a non-negligible amount of 12 % even though it was barely determined. As, in addition, its value appeared to be reasonable, see further below, this constant was retained in the final fit. The resulting spectroscopic parameters are given in Table 6 together with the most recent previous values by Müller et al. (2000).

Table 6: Spectroscopic parameters<sup>a</sup> (MHz) of C<sub>2</sub>H in comparison to previous values.

Parameter	present value	Müller et al. (2000)
$B$	43674.5177 (13)	43674.5289 (12)
$D \times 10^3$	105.515 (53)	105.687 (51)
$H \times 10^6$	−0.42 (32)	0.32 (32)
$\gamma$	−62.6103 (45)	−62.6029 (43)
$\gamma^D \times 10^3$	−2.227 (250)	−2.313 (255)
$b_F$	44.4788 (82)	44.4922 (183)
$b_F^D$	—	−0.0100 (38)
$c$	12.2389 (232)	12.2256 (261)
$C$	−0.0087 (53)	—

<sup>a</sup> Numbers in parentheses are one standard deviation in units of the least significant figures.

The most striking feature in the comparison of the present C<sub>2</sub>H rest frequencies with those from Gottlieb et al. (1983) is that the latter are on average 28.6 kHz higher in frequency, ranging from complete agreement to 51 kHz for the individual HFS components. Moreover, the deviations are a few times the uncertainties reported by Gottlieb et al. (1983) for some lines. In fact, employing the present spectroscopic parameters given in Table 6, the Gottlieb et al. (1983) data are reproduced to only 3.6 times their reported uncertainties on average. We suspect that the LSR velocity of the source north of Orion-KL used in Gottlieb et al. (1983) was not as well known as the authors assumed and that for the laboratory measurements the frequency determinations were slightly off or the estimates of the uncertainties were slightly too optimistic.

The present rest frequencies have been reproduced to 0.6 times the uncertainties, slightly better still for the  $N=1-0$  transition, suggesting that the uncertainties in Table 5 and even more so in Table 4 have been judged somewhat too conservatively. On the other hand, uncertainties in the LSR velocity may justify such a conservative error estimate. The  $N=3-2$  lines from Sastry et al. (1981) have been reproduced to better than 18 kHz, which is much better than the  $\sim 45$  kHz with which these data were reproduced in Müller et al. (2000). In other words, these  $N=3-2$  rest frequencies are much better compatible with the present  $N=1-0$  and  $N=2-1$  rest frequencies than with those from Gottlieb et al. (1983). The submillimetre data from Müller et al. (2000) are at somewhat higher frequencies

and quantum numbers such that both present and previous spectroscopic parameters in Table 6 reproduce these data on average to about 0.6 times the reported uncertainties.

While frequency deviations of a few tens of kHz may possibly be neglected in observations of hot cores or similar sources, the deviations are rather considerable for investigations into the dynamics of dark clouds as in the present study. The deviations are also reflected in the small ( $\sim 11$  kHz) differences in the rotational constant  $B$ , see Table 6. Nevertheless, these deviations are more than four times the combined uncertainties and thus clearly significant. It is worth noting that the  $B$  value in Müller et al. (2000) is determined essentially by the data from Gottlieb et al. (1983). The slightly higher  $D$  value from the present study, just outside the combined uncertainties, compensates the change in  $B$  to some degree for the submillimetre lines. The sextic term  $H$  is essentially the same as in the previous study, still not determined with significance, but probably of the right order of magnitude.

Changes in the fine structure parameters and in the larger hyperfine structure parameters are essentially insignificant. The distortion correction  $b_F^D$  had been used in the previous fit of Müller et al. (2000) since its inclusion improved the Gottlieb et al. (1983) data to be reproduced on average from 1.31 times the uncertainties to 0.93 times the uncertainties. In present trial fits its value was determined as  $-0.0021$  (33) MHz. The magnitude of the ratio  $b_F^D/b_F$  is now much closer to that of  $\gamma^D/\gamma$ , but still much bigger than that of  $D/B$ . However, the uncertainty was larger in magnitude than the value, and the inclusion of the parameter in the fit improved the quality of the fit only insignificantly. The term  $b_F^D$  was consequently omitted from the final fit. The inclusion of the <sup>1</sup>H nuclear spin-rotation term  $C$  in the present fit requires some explanation. This term is usually small and negative and frequently scaling with the rotational constant is the dominant contribution to its size. The C<sub>2</sub>H value of  $-8.7$  (53) kHz agrees within its large uncertainty with the experimental one of  $-4.35$  (5) kHz for HCN (Ebenstein & Muentner 1984) and with the calculated values of  $-4.80$  kHz and  $-5.55$  kHz for HCN and HCO<sup>+</sup> (Schmid-Burgk et al. 2004) and appears thus to be reasonable as these species have fairly similar rotational constants.

## 5. Non-LTE hyperfine populations

In this Section we consider the evidence for non-LTE populations in the hyperfine levels sampled by our observations. We first compare the observed intensity ratios of C<sub>2</sub>H in L1498 and CB246 with the predictions of simple LTE models and find that while real deviations from LTE populations are present, the LTE assumption is an approximation which is useful for many purposes. We then consider a Monte Carlo radiative transfer program for the case of C<sub>2</sub>H and show that the observed deviations can be approximately understood with an educated guess at the (unknown) C<sub>2</sub>H collisional rates.

### 5.1. Single- and two-layer models

We note first that for the case of LTE between different hyperfine levels (i.e. all transitions of a given multiplet have the same excitation temperature), we expect that for a homogeneous slab, the ratio of line intensities of two transitions  $R_{ij}$  is given by:

$$R_{ij} = \frac{1 - \exp(-f_i \tau)}{1 - \exp(-f_j \tau)} \quad (2)$$

where  $\tau$  is the total transition optical depth and  $f_i$  is the relative line strength of the  $i$ -th component as e.g. in Table 4. Thus, as the optical depth varies, the expected  $R_{ij}$  varies from  $f_i/f_j$  to unity and for two different pairs of transitions, one can derive a curve in the plane ( $R_{ij}, R_{kl}$ ). In Fig. 9, we give for various combinations of transitions in the  $N=1-0$  transition our observed line ratios compared with the result expected on the basis of equation 2, and in Fig. 10, we show analogous results for the  $N=2-1$  line. We see that the observed intensity ratios in C<sub>2</sub>H(1-0) are not consistent with equation 2 although the deviations are not large. In particular, we note in Fig. 9 that ratios such as  $R_{32}$  (upper right panel) at some positions attain values below the optically thin expected value of 0.5. More significantly perhaps the observed ratio  $R_{34}$  (bottom right panel) of the 83728 and 87401 MHz lines which have essentially the same line strength is typically of order 0.8–0.9 and at almost all positions less than unity. These differences are not significant at individual positions, but appear to be significant statistically. The results in Fig. 9 are for L1498, but similar trends hold for CB246.

Fig. 10 shows analogous results for C<sub>2</sub>H(2-1). There are fewer positions but again, we see significant deviations from the homogeneous single layer prediction of equation 2. The ratio  $R_{32}$  (upper left panel) of the 174667 and 174663 MHz lines is typically between 0.5 and 0.6 as compared to the optically thin LTE prediction of 0.66. These differences are small but appear to be significant.

Equation 2 assumes a homogeneous one-dimensional solution of the transfer equation and it is clear that for a real prestellar core, gradients in both temperature and density are present. Indeed observations of some cores in strong ground state transitions such as HCO<sup>+</sup>(1-0) are complicated by absorption in a foreground layer whose excitation appears to be essentially that of the cosmic background (Tafalla et al. 1998). In the particular case of C<sub>2</sub>H towards L1498, the “self-absorption” observed in the 87316 MHz line (see Fig. 4) suggests that something of this sort may occur also for C<sub>2</sub>H. In view of this, we have also considered a two-layer model of the type discussed by Myers et al. (1996) with background ( $b$ ) and foreground ( $f$ ) layers having excitation temperatures  $T_{\text{ex},b}$  and  $T_{\text{ex},f}$  and optical depths  $\tau_f$  and  $\tau_b$  respectively. We then find for the emergent intensity of  $i$ -th component:

$$T_{\text{mb},i} = J(T_{\text{ex},f})[1 - e^{-\tau_{f,i}}] + J(T_{\text{ex},b})[1 - e^{-\tau_{b,i}}]e^{-\tau_{f,i}} - J(T_{\text{bb}})[1 - e^{-\tau_{b,i}-\tau_{f,i}}] \quad (3)$$

where

$$J(T) = \frac{T_0}{\exp(T_0/T) - 1} \quad (4)$$

is the Planck-corrected brightness temperature and  $T_{\text{bb}} = 2.73$  K is the temperature of the cosmic background.  $T_0 \equiv h\nu/k$ , where  $\nu$  is the transition frequency and  $h$  and  $k$  represent Planck’s and Boltzmann’s constants respectively. The optical depth of the  $k$ -layer ( $k = f, b$ ) for the  $i$ -th component is defined as  $\tau_{k,i} \equiv \tau_0 f_i \phi_i$ , where  $f_i$  is again the relative intensity and  $\phi_i$  is the profile which we assume as gaussian, that is

$$\phi_i = 2 \sqrt{\frac{\ln 2}{\pi}} \exp \left\{ -\frac{4[V - (-1)^m \langle V_{k,i} \rangle]^2 \ln 2}{\sigma^2} \right\} \quad (5)$$

with  $m = 0$  for the foreground layer and  $m = 1$  for the background layer. We have included in Fig. 9 and 10 predictions



based on our two-layer model varying  $T_{\text{ex},f}$  and we derive the dashed curves using equation 3. We see from this that the effect of “foreground layers” is to increase ratios such as  $R_{32}$  in some cases to values of order unity. Essentially, this is due to absorption of the strong 87316 MHz line (component 2). One sees from both Fig. 9 and 10 that this is not what is required to fit the observed data and in fact the two-layer models are a poorer approximation to the observed intensity ratios than the single-layer LTE model. We thus conclude that understanding the observed line ratios requires a proper non-LTE treatment.

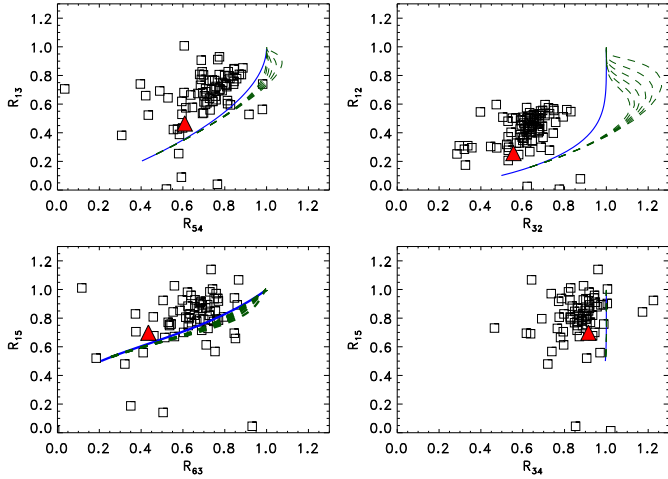


Fig. 9: Ratio of the integrated intensities of some couples of components of C<sub>2</sub>H(1–0) in L1498, where  $R_{ij}$  represents the ratio between  $\int T_{\text{mb},i} dV$  and  $\int T_{\text{mb},j} dV$ . Observational data, *black empty squares*; one-layer model, *blue solid curve*; two-layer model with different  $T_{\text{ex},f}$ , *green dashed curves*; results from Monte Carlo model, *red filled triangles*. The typical errors on the ratios are of the order of  $8.5 \times 10^{-2}$ .

## 5.2. Monte Carlo treatment of radiative transfer in the C<sub>2</sub>H rotational transitions

The two-layer model, with its assumption of the same excitation temperature for all hyperfine components in each layer and its discontinuous jump in conditions between the two emitting regions, misses an important part of the complex pattern of level populations responsible for the emission in C<sub>2</sub>H(1–0). As can be seen in Fig. 4, the hyperfine components of C<sub>2</sub>H(1–0) are simultaneously subthermal and optically thick in both L1498 and CB246, and under these conditions, the excitation temperature of each component is determined by a delicate balance between collisions and trapping. This balance will be different for each transition depending on its particular optical depth, and it will therefore give rise to differences in excitation between the components of the  $N=1-0$  multiplet. The large optical depth of the lines, in addition, makes the emission from each component originate in gas at different depth in the core, and this also contributes to differences in the observed line intensities. Such complex interplay between excitation and optical depth effects cannot be treated accurately with the two-layer model, and its analysis requires a more sophisticated numerical scheme. In this Section, we present the result of a (partial) solution to the C<sub>2</sub>H radiative transfer problem using the same Monte Carlo code used

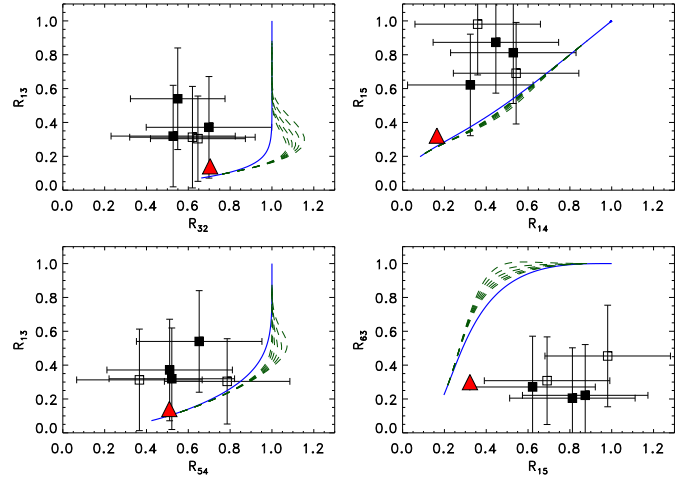


Fig. 10: Ratio of the integrated intensities of some couples of components of C<sub>2</sub>H(2–1), where  $R_{ij}$  represents the ratio between  $\int T_{\text{mb},i} dV$  and  $\int T_{\text{mb},j} dV$ . Observational data, *black empty squares* for L1498 and *black filled squares* for CB246; one-layer model, *blue solid curve*; two-layer model with different  $T_{\text{ex},f}$ , *green dashed curves*; results from Monte Carlo model for L1498, *red filled triangles*.

in Tafalla et al. (2004, 2006) to analyse the emission from a number of molecular species in the L1498 and L1517B cores.

As the modelling of the L1498 emission in Tafalla et al. (2004, 2006) already fixed the physical description of this core (radial profiles of density, temperature, and velocity), the only parameter left free to model the C<sub>2</sub>H emission is the radial profile of abundance. Unfortunately, the C<sub>2</sub>H analysis is limited due to the lack of known collision rates for the species, and this forces us to make an educated guess of this important set of coefficients. Following Turner et al. (1999), we approximate the collision rates of C<sub>2</sub>H using those for HCN calculated by Green & Thaddeus (1974). From these rates, which do not include hyperfine structure, we derive a new set of rates with hyperfine structure assuming that the new rates are simply proportional to the degeneracy of the final state (Guilloteau & Baudry 1981, Lique et al. 2009). Additional  $\Delta N = 0$  rates were included by following the recipe from Turner et al. (1999), and a total of 30 levels with 37 transitions (up to  $N = 7$  and an energy equivalent to 120 K) were used in the calculation.

Following the analysis of other species in L1498, the goal of our C<sub>2</sub>H modeling was to fit simultaneously the combined radial profile of  $N=1-0$  integrated intensity together with the central spectra of the different components of the  $N=1-0$  and  $N=2-1$  multiplets, assuming a uniform kinetic temperature of 10 K (as derived from a non-LTE analysis of the NH<sub>3</sub> data by Tafalla et al. 2004). A first set of model runs using the collision rates described before predicted excitation temperatures that were too high in the outer core layers, a situation that is inconsistent with the self absorbed profile seen in the thickest  $N=1-0$  component (Fig. 4). This inconsistency indicated that the guessed C<sub>2</sub>H collision rates were too large, and that they should be significantly reduced in order to match the observations. To avoid introducing artifacts in the relative excitation of the hyperfine components, the collision rates were reduced dividing them by a global factor of 3. With these corrected collision rates, a fit was achieved by assuming a constant C<sub>2</sub>H abundance with respect to H<sub>2</sub> of  $8 \times 10^{-9}$  and a central depletion region of radius

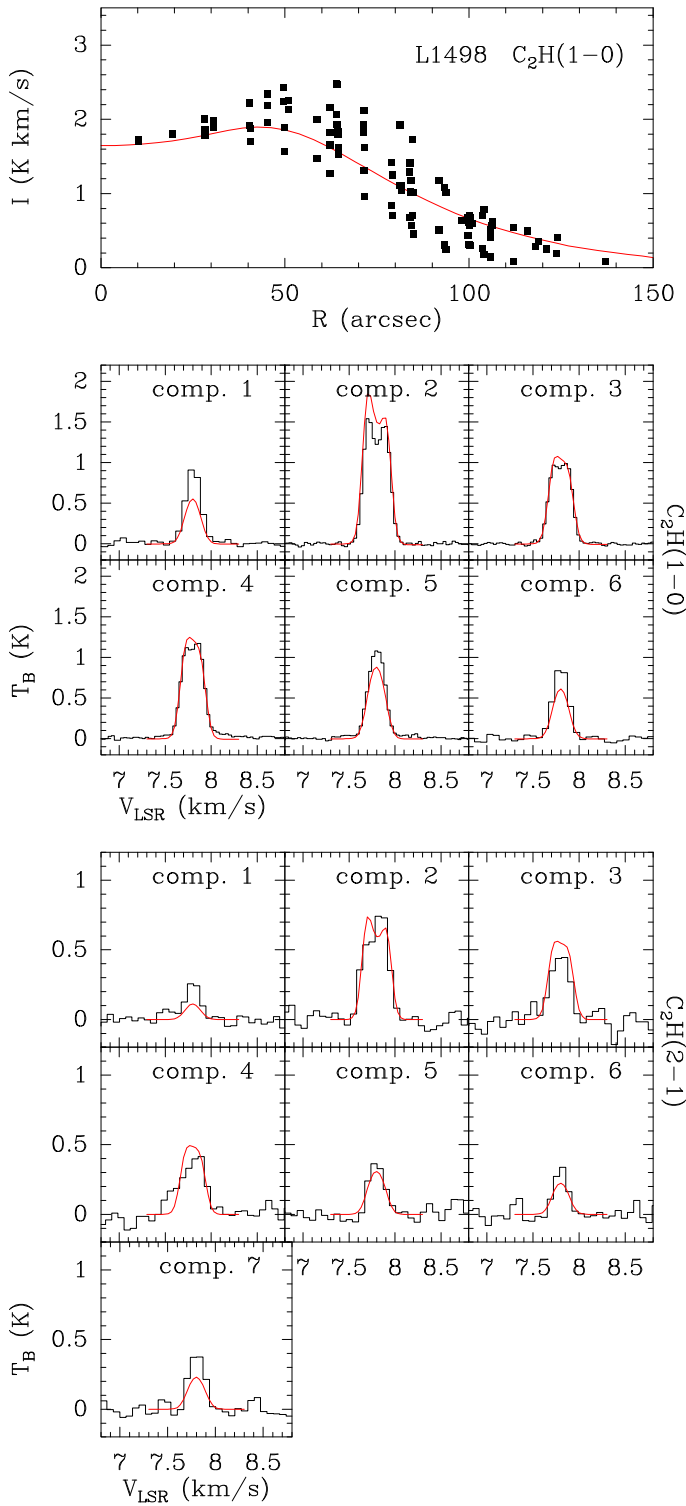


Fig. 11: Comparison between observations and our best fit Monte Carlo model of the C<sub>2</sub>H emission in L1498. *Top panel*: radial profile of observed C<sub>2</sub>H(1–0) intensity integrated over all hyperfine components (*filled squares*) and model prediction for a constant abundance core with a central depletion hole (*solid red line*). *Middle panels*: emerging spectra for each component of the C<sub>2</sub>H(1–0) multiplet (*black histograms*) and predictions for the same best fit model (*solid red lines*). *Bottom panels*: same as middle panels but for the components of the C<sub>2</sub>H(2–1) multiplet. Note the reasonably good fit of all observables despite the use of highly approximated collisional rates (see text).

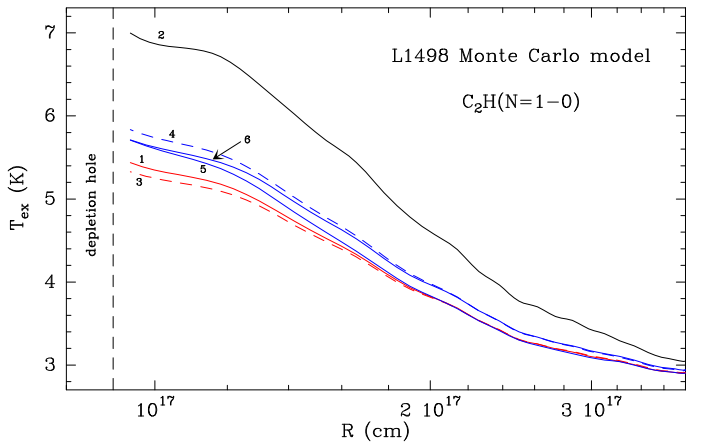


Fig. 12: Radial profile of excitation temperature for each hyperfine component of C<sub>2</sub>H(1–0) as predicted by our best fit Monte Carlo model (each component is labelled according to the ordering in Table 3). Note the gradual drop of  $T_{\text{ex}}$  with radius, which is caused by the combined decrease in collisional excitation and photon trapping towards the outer core. The different hyperfine components have different  $T_{\text{ex}}$  depending mostly on trapping effects (see text for a full discussion).

$9 \times 10^{16}$  cm inside which the C<sub>2</sub>H abundance is negligible ( $10^{-4}$  times the outer value), similar to that of other species in L1498, see Tafalla et al. 2006. The results of this model are shown in Fig. 11 (red lines) superposed to observations (black histograms and squares). As it can be seen, the model fits reasonably well both the radial profile of  $N=1-0$  intensity and the spectra of most components in both the  $N=1-0$  and  $N=2-1$  multiplets. The model in addition, fits reasonably well the observed ratios of line pairs presented in Fig. 9.

If our Monte Carlo model fits the observed C<sub>2</sub>H emission, we can use it to analyze the excitation of the different  $N=1-0$  components and understand the origin of the observed line ratios. This is best done by studying the radial profile of excitation temperature, which is presented in Fig. 12. As the figure shows, the  $T_{\text{ex}}$  of each component systematically decreases with radius, from about 6 K in the core interior to a value close to the cosmic background temperature near the core edge. The figure, in addition, shows that at each radius, the  $T_{\text{ex}}$  of the different components can differ by as much as 1 K, and that component 2 is significantly more excited than the rest. These differences in excitation over the core and among components could in principle result from differences in the contribution of collisions or from photon trapping, and to disentangle the two effects we have run an alternative model having a factor of  $10^4$  lower abundance. This optically thin case also presents an outward drop in  $T_{\text{ex}}$ , this time entirely due to the effect of collisions, but it predicts excitation temperatures in the core interior that are about 1 K lower than for the best fit model. In addition, component 2 in this thin case has a  $T_{\text{ex}}$  comparable to that of the other components, and the overall scatter of  $T_{\text{ex}}$  among all components does not exceed 0.5 K. This decrease in the excitation when the lines become thin indicates that in the best fit model the  $N = 1$  level populations are significantly enhanced by trapping of  $N = 1-0$  photons. The higher excitation of component 2, in particular, appears as an extreme case of trapping: this component has the largest relative intensity and therefore is the most sensitive one to optical depth effects. Its sensitivity to trapping makes it the brightest line of the multiplet despite suffering from self absorption at the line cen-

tre. Differential line trapping seems also responsible for the different intensity of components 3 and 4, which would otherwise be equally bright because of their equal Einstein A coefficient and upper level statistical weight. As Fig. 12 shows, component 4 has an  $\approx 0.5$  K higher  $T_{\text{ex}}$  in the inner core, and this is most likely the result of enhanced trapping due to an overpopulation of the  $N, J, F = 0, 1/2, 1$  level, where most  $N=1-0$  transitions end (except for components 3 and 6).

In summary, our model shows that most excitation “anomalies” of the hyperfine components in the  $N=1-0$  multiplet can be explained as resulting from the different balance between collisions and trapping expected for lines of very different intrinsic intensities under conditions of subthermal excitation and high optical depth. Further work on this issue requires an improved set of collision rates for C<sub>2</sub>H, and we encourage collision rate modelers to consider this species for future computations.

## 6. Column density and abundance estimate

Deriving a column density for C<sub>2</sub>H requires an estimate of the excitation temperature. This as we see in the Monte Carlo calculations discussed above depends on the line transfer and hence on position within the core. However a reasonable approximation to the column density can be obtained assuming a homogeneous layer with constant excitation temperature. We have verified this assumption for the case of L1498 using the Monte Carlo program.

The excitation temperature  $T_{\text{ex}}$  can be inferred (*method 1*) from an LTE fit to the hyperfine components of either the  $N=1-0$  or  $N=2-1$  lines assuming unity beam filling factor and using the measured intensity of optically thick transitions. An independent measure can be obtained (*method 2*) from the ratio of intensities of low line strength transitions of the  $N=2-1$  and  $N=1-0$  lines assuming them to be optically thin. We summarize in Table 7 the excitation temperatures derived using these different approaches for the positions where we have  $N=2-1$  data available. From Table 7 we see that in both sources, the excitation temperature appears to be between 3.8 and 4.9 K. We will assume an excitation temperature of 4 K in the following for all positions.

Table 7: Values of  $T_{\text{ex}}$  [K] derived using the two methods.

$\alpha, \delta$ offsets	<i>method 1</i>		<i>method 2</i>
["", ""]	C <sub>2</sub> H(1-0)	C <sub>2</sub> H(2-1)	
L1498			
0,0	4.0 ± 0.1	4.6 ± 0.6	4.2 ± 0.6
60,-40	4.1 ± 0.1	4.3 ± 0.8	4.4 ± 0.5
CB246			
0,0	4.1 ± 0.1	4.9 ± 1.0	4.4 ± 0.9
15,-30	4.1 ± 0.3	4.4 ± 0.7	4.4 ± 0.4
-60,15	4.0 ± 0.2	3.9 ± 0.4	3.8 ± 0.6

For an optically thin C<sub>2</sub>H(1-0) line, one can derive the column density,  $N(\text{C}_2\text{H})$ , through the formula:

$$N(\text{C}_2\text{H}) = \frac{8\pi\nu_{ji}^3}{c^3} \frac{Q}{A_{ji}g_j} \frac{e^{E_j/kT_{\text{ex}}}}{e^{h\nu_{ji}/kT_{\text{ex}}} - 1} \frac{\int T_{\text{mb}} dv}{J(T_{\text{ex}}) - J(T_{\text{bg}})} \quad (6)$$

where  $\nu_{ji}$  is the transition frequency,  $c$  the speed of light,  $A_{ji}$  the Einstein coefficient,  $g_j$  the statistical weight,  $E_j$  the energy of

the upper level,  $T_{\text{ex}}$  the excitation temperature,  $\int T_{\text{mb}} dv$  the integrated intensity,  $J(T)$  as defined in eq. 4 and  $Q = \sum_{j=0}^{\infty} g_j e^{-E_j/kT_{\text{ex}}}$  is the partition function. The integral in equation 6 is over all six hyperfine components. In practise, the stronger components of the line are sometimes thick and we have hence integrated only over the 87284 MHz and 87446 MHz lines (components 1 and 6 in Table 4) and divided the result by the sum of their line strengths (0.085) in order to evaluate the integral in equation 6.

We need to compare this with the molecular hydrogen column density  $N(\text{H}_2)$  and we do this using the mm dust emission (from Tafalla et al. 2004 for L1498 and from this work, see Sect. 2.3, for CB246). We assume here in both sources a dust grain opacity of  $0.005 \text{ cm}^2 \text{ g}^{-1}$  of dust and a dust temperature of 10 K, as in Sect. 3.4.

We also evaluated the column densities and the abundances of N<sub>2</sub>H<sup>+</sup> and CO for CB246 (using our data, see Sect. 2.2) and for L1498 (using data from Tafalla et al. 2004). We derived  $N(\text{N}_2\text{H}^+)$  following the same procedure as for  $N(\text{C}_2\text{H})$ . Thus, if the stronger components of N<sub>2</sub>H<sup>+</sup>(1-0) are thick then we integrated only over the isolated component ( $F'_1, F' \rightarrow F_1, F = 1, 2 \rightarrow 0, 1$ ), dividing the result by its line strength (0.111). In the case of C<sup>18</sup>O, we used directly equation 6 to calculate  $N(\text{C}^{18}\text{O})$  and  $N(\text{CO})$  assuming  $[^{16}\text{O}]/[^{18}\text{O}] \sim 560$  (Wilson & Rood 1994). We give in Table 8 abundance estimates that we have made at selected positions in L1498 and CB246.

Table 8: Molecular abundances in L1498 and CB246.

$\alpha, \delta$ offsets ["", ""]	[C <sub>2</sub> H]/[H <sub>2</sub> ] [10 <sup>-8</sup> ]	[N <sub>2</sub> H <sup>+</sup> ]/[H <sub>2</sub> ] [10 <sup>-10</sup> ]	[CO]/[H <sub>2</sub> ] [10 <sup>-5</sup> ]
L1498			
0,0	0.8 $\pm$ 0.1	1.9 $\pm$ 0.4	0.5 $\pm$ 0.1
-40,20	1.1 $\pm$ 0.3	1.8 $\pm$ 0.5	0.8 $\pm$ 0.2
60,-40	1.5 $\pm$ 0.4	2.4 $\pm$ 0.7	1.1 $\pm$ 0.3
CB246			
0,-15	1.0 $\pm$ 0.3	3.1 $\pm$ 1.6	0.9 $\pm$ 0.2
-60,15	1.2 $\pm$ 0.5	2.4 $\pm$ 1.7	1.0 $\pm$ 0.3
-60,60	1.0 $\pm$ 0.3	1.2 $\pm$ 0.9	1.3 $\pm$ 0.4
-30,15	1.0 $\pm$ 0.2	3.0 $\pm$ 1.2	1.6 $\pm$ 0.5

In Fig. 13, we show the plot of C<sub>2</sub>H, N<sub>2</sub>H<sup>+</sup> and CO column density against H<sub>2</sub> column density at different positions in both sources. We find that for column densities  $N(\text{H}_2) \lesssim 2 \times 10^{22} \text{ cm}^{-2}$ ,  $N(\text{C}_2\text{H})$  is proportional to  $N(\text{H}_2)$  but, in L1498, for higher values of  $N(\text{H}_2)$ , this proportionality breaks down and  $N(\text{C}_2\text{H})$  seems to saturate at a value of  $\sim 2.2 \times 10^{14} \text{ cm}^{-2}$ . This is likely due to depletion of C<sub>2</sub>H in the high density core of L1498 as already suggested by the maps in Fig. 1, the cuts in Fig. 3 and the Monte Carlo modeling. This behaviour is in complete analogy with several other species including the carbon rich molecule C<sub>3</sub>H<sub>2</sub> (Tafalla et al. 2006).

On the other hand, for  $N(\text{H}_2)$  less than  $2 \times 10^{22} \text{ cm}^{-2}$ , we find that the ratio  $N(\text{C}_2\text{H})/N(\text{H}_2)$  is constant corresponding to a constant C<sub>2</sub>H abundance in the low density part of the core. This corresponds to an average estimated C<sub>2</sub>H abundance relative to H<sub>2</sub> of  $(1.0 \pm 0.3) \times 10^{-8}$  in L1498 and  $(0.9 \pm 0.3) \times 10^{-8}$  in CB246. Our C<sub>2</sub>H abundances estimate for L1498 using eq. 6 agrees to within 20% with the Monte-Carlo estimate discussed in Section 5.2. It is noteworthy and somewhat surprising to us that the C<sub>2</sub>H abundances are so similar in cores of differing characteristics.

A more strict correlation over the whole range of observed H<sub>2</sub> column density is shown by the ratio  $N(\text{N}_2\text{H}^+)/N(\text{H}_2)$  which corresponds to an average estimated N<sub>2</sub>H<sup>+</sup> abundance relative to H<sub>2</sub> of  $(1.8 \pm 1.2) \times 10^{-10}$  in L1498 and  $(1.8 \pm 0.8) \times 10^{-10}$  in CB246. C<sup>18</sup>O behaves differently showing a rather constant value of its column density over the  $N(\text{H}_2)$  range corresponding to  $N(\text{CO}) = (2.0 \pm 0.4) \times 10^{17} \text{ cm}^{-2}$  in CB246 and  $(2.1 \pm 0.3) \times 10^{17} \text{ cm}^{-2}$  in L1498, while the average abundance relative to H<sub>2</sub> is  $(1.3 \pm 0.6) \times 10^{-5}$  in L1498 and  $(1.5 \pm 0.4) \times 10^{-5}$  in CB246.

One difference between CB246 and L1498 is that the  $N(\text{H}_2)$  peak (see Fig. 13) is a factor 1.33 smaller in CB246 and indeed does not reach values for which large depletion is noted in L1498. However, our map in C<sup>18</sup>O(2–1) (see lower panel of Fig. 2) as well as the cuts shown in Fig. 6 suggest to us that some CO depletion does occur in CB246.

## 7. Discussion

In this study, we have compared two cores of rather different characteristics. L1498 is embedded in the Taurus complex with a total dimension of  $2.6 \times 2.0$  arc minutes (Caselli et al. 2002) corresponding to  $0.10 \times 0.08$  parsec at the distance of 140 parsec (Elias, 1978). CB246 is an isolated globule with dimensions of  $7.8 \times 4.5$  arc minutes corresponding to  $0.45 \times 0.26$  parsec at our adopted distance of 200 parsec. It is thus perhaps not surprising that the non-thermal component of the line width, obtained from the observed line widths corrected for thermal broadening (see e.g. Caselli & Myers 1995), is  $0.23 \text{ km s}^{-1}$  in CB246 as compared to  $0.14 \text{ km s}^{-1}$  in L1498. However, apart from that, many characteristics of these two objects seem similar as discussed below.

### 7.1. Non-LTE effects

One of our aims was to test for non-LTE effects in C<sub>2</sub>H if any in the hope that this could lead to a better understanding of physical conditions in cores. Our results show that non-LTE effects do occur and they are qualitatively similar in the two cores. With our Monte Carlo radiative transfer program, we have shown that one can qualitatively understand their nature in terms of trapping of individual components of the  $N=1-0$  and  $N=2-1$  lines. These calculations also show that reasonable estimates of parameters such as the C<sub>2</sub>H column density can be obtained using a simple one-layer homogeneous model with constant excitation temperature. Given that real cores are not spherically symmetric, this is a useful simplification. Clearly, more refined models will eventually be useful but equally clearly, this requires computations of collisional rates for C<sub>2</sub>H along the lines of those carried out by Monteiro and Stutzki (1986) for HCN.

### 7.2. Chemistry

There has been significant recent work on the chemistry of prestellar cores (see e.g. Aikawa et al. 2003, 2005, Lee et al. 2004, Flower et al. 2006, Akyilmaz et al. 2007). These studies follow the evolution of molecular abundances in a collapsing prestellar core as a function of time and initial conditions. For example, the Aikawa et al. (2005) model, a model with  $\alpha$ , the ratio of gravitational to pressure force, equal to 1.1, predicts a  $[\text{C}_2\text{H}]/[\text{H}_2]$  abundance ratio of  $4 \times 10^{-9}$  at a radius of 10000 AU (i.e. outside the depletion hole) or a factor of roughly 3 smaller than our observed value but there are a variety of factors which influence this estimate as we now discuss. One factor

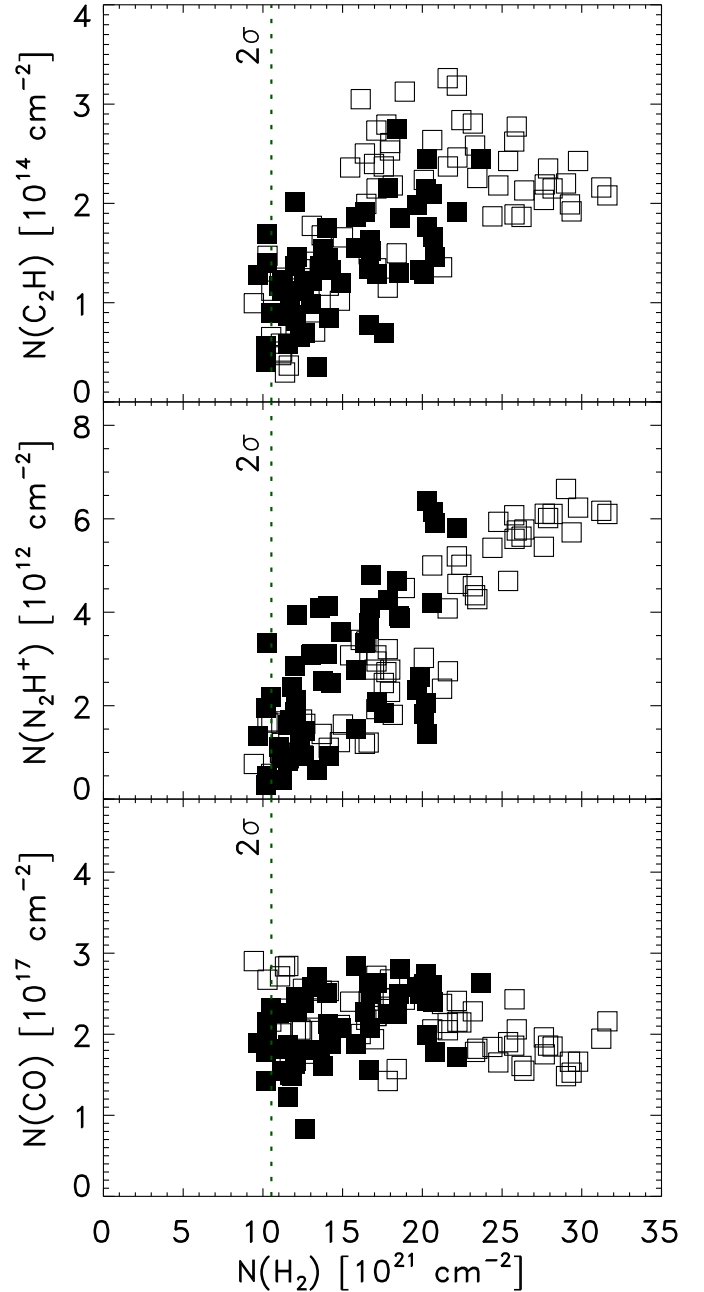


Fig. 13: Plot of the column density of C<sub>2</sub>H, N<sub>2</sub>H<sup>+</sup> and CO against the H<sub>2</sub> column density for L1498 (*open squares*) and CB246 (*filled squares*). The dotted line represents the  $2\sigma = 6 \text{ mJy}$  limit of the continuum emission. Data for N<sub>2</sub>H<sup>+</sup> and CO for L1498 are from Tafalla et al. (2004).

is that results are sensitive to the degree of depletion onto grain surfaces which, in turn, depends on the effective grain cross section. Another important parameter is the effective  $[\text{C}]/[\text{O}]$  ratio in the gas phase because this is critical for the formation of C-rich species such as C<sub>3</sub>H<sub>2</sub>, HC<sub>3</sub>N, and C<sub>2</sub>H (see Terzieva & Herbst 1998, Akyilmaz et al. 2007). A  $[\text{C}]/[\text{O}]$  ratio close to unity can occur when a large fraction of the available oxygen condenses out in the form of water ice on grain surfaces. In this situation, the model calculations suggest that CO takes the lion's share of

both carbon and oxygen in the gas phase and that, as a result, little oxygen is left in atomic or molecular form.

The results of Terzieva & Herbst (1998) show in particular that the C<sub>2</sub>H abundance can change by an order of magnitude due either to the assumptions concerning [C]/[O] or due to assumptions concerning the rates of certain neutral-neutral reactions. We find in contrast that the observed C<sub>2</sub>H abundance does not seem to change greatly as a function of position and in fact, to a reasonable approximation, C<sub>2</sub>H follows the C<sup>18</sup>O distribution. Where CO appears to be depleted in L1498, C<sub>2</sub>H seems to be depleted also and this also seems to be true for CB246 although the depletion holes are smaller. To some extent, we presume that this reflects the fact that CO is the main source of gas phase carbon in cores. When CO depletes, there is less carbon available to form species with 2 or more C atoms. It is striking also that we derive very similar C<sub>2</sub>H abundances in the two cores which we have studied. This may be due to chance but it is interesting that our estimated C<sub>2</sub>H abundance is similar to that derived in TMC1 and L183 (see Table 2 of Terzieva and Herbst 1998).

It is also worth noting that C<sub>2</sub>H, being a radical, is subject to destruction by atomic oxygen and nitrogen. Thus from the UMIST database (Woodall et al. 2007), one finds that C<sub>2</sub>H reacts with O forming CO and CH at a rate of  $1.7 \times 10^{-11} \text{ cm}^3 \text{ s}^{-1}$  and the rate for atomic N is similar. This compares with a rate for depletion onto dust grain surfaces of roughly  $10^{-17} n_{\text{H}} \text{ s}^{-1}$  where  $n_{\text{H}}$  is the hydrogen nucleon density in  $\text{cm}^{-3}$  and a rate of  $10^{-9} \text{ cm}^3 \text{ s}^{-1}$  for reactions with ions such as C<sup>+</sup> and H<sub>3</sub><sup>+</sup>. For an ionization degree of  $10^{-8}$ , which is fairly typical in cores (see Fig. 5 in Walmsley et al. 2004), reactions with ions and depletion onto grain surfaces are competitive with one another. Destruction by atomic oxygen and nitrogen will dominate if the abundances of these species exceeds about  $6 \times 10^{-7}$  relative to hydrogen. The atomic abundances are hence critical for the C<sub>2</sub>H abundance and it is presumably for this reason (at least as far as O is concerned) that the results of model calculations show C<sub>2</sub>H to be very sensitive to the gas phase [C]/[O] ratio (e.g. Terzieva and Herbst 1998, their Table 5). In fact, the only one of their model predictions for C<sub>2</sub>H which compares reasonably with our observed values has a [C]/[O] ratio of 0.8 (run 3 in their Table 5). We conclude that high [C]/[O] gas phase ratios (and consequently a low atomic O abundance) are part of the explanation of the relatively high observed C<sub>2</sub>H abundance. This presumably implies a scenario with a large fraction of oxygen locked-up in the form of water ice on grain surfaces (see e.g. Hollenbach et al. 2009).

### 7.3. C<sub>2</sub>H as a magnetic field probe

As mentioned in the Introduction, C<sub>2</sub>H is potentially capable of being used to measure the Zeeman effect. The CN(1–0) transition has been successfully used for this purpose (Falgarone et al. 2008) and superficially at least, C<sub>2</sub>H has similar characteristics to CN (they are iso-electronic). We have therefore used the results of Crutcher et al. (1996) together with the Zeeman splitting calculations of Bel & Leroy (1998) to infer the expected RMS sensitivity to magnetic field  $\sigma_B$  of a C<sub>2</sub>H measurement at the intensity peak in L1498 for an integration time  $t_{\text{int}}$ . Thus we take

$$\sigma_B \approx \frac{2}{Z} \frac{T_{\text{sys}}}{T_A^*} \frac{\Delta\nu_{\text{FWHM}}}{\delta\nu t_{\text{int}}} \quad (7)$$

In this equation, we use our observed line intensities  $T_A^*$ , system temperature  $T_{\text{sys}}$ , the spectral resolution  $\delta\nu$  and width  $\Delta\nu_{\text{FWHM}}$

for L1498 as well as the expected Zeeman splitting factors  $Z$ , in  $\text{Hz } \mu\text{G}^{-1}$ , from Bel and Leroy (1998) to derive expected values of  $\sigma_B$  for all six C<sub>2</sub>H(1–0) transitions. The results, for an hour of integration, are given in Table 9 where we see component 5 of C<sub>2</sub>H is the most favorable for detecting Zeeman splitting and that, as for CN, there is a large variation of expected splitting between components. This latter property is of fundamental importance for the purpose of eliminating instrumental effects such as beam squint.

Table 9: Expected values of  $\sigma_B$  for all six C<sub>2</sub>H(1–0) transitions in L1498 at the offset (60, –40) for an hour of integration and a spectral resolution equal to 40 kHz.

comp. no.	$Z$ [Hz $\mu\text{G}^{-1}$ ]	$T_A^*$ [K]	$\Delta\nu_{\text{FWHM}}$ [kHz]	$\sigma_B$ [ $\mu\text{G}$ ]
1	2.6	0.9	80	740
2	0.7	1.4	100	2210
3	2.3	1.0	90	860
4	0.93	1.1	95	1990
5	2.8	1.1	85	590
6	0.93	0.9	75	1860

See Table 4 for component labels.

One sees also that without a considerable improvement in system temperature, it will be difficult to get below  $3\sigma_B$  limits of 200  $\mu\text{G}$ . There have been claims of fields of this order however (e.g. Shinnaga et al. 1999); Crutcher (1999) found a reasonable fit to the Zeeman data available at the time of  $B_{\text{los}} = 80 \times n_4^{0.46} \mu\text{G}$  with  $n_4 = 10^{-4} n(\text{H}_2)$  which would suggest that fields of order 200  $\mu\text{G}$  are reasonable in sources like L1498. We conclude therefore that fields of this order may be detectable using C<sub>2</sub>H but it is extremely difficult with current sensitivities. On the other hand, in more general, prospects do not seem worse than with CN.

## 8. Conclusions

We have carried out a study of the behaviour of the abundance of C<sub>2</sub>H toward two starless cores with contrasting properties, L1498 and CB246. The main conclusions of our work are the following:

1. In L1498, C<sub>2</sub>H shows a distribution similar to that observed in other species attributed to depletion onto grain surfaces in the central region; by contrast, in CB246 the dust and the C<sub>2</sub>H emission have similar distributions.
2. The two cores show a clear signature for deviations from LTE populations in C<sub>2</sub>H: spectra in most positions deviate from expectations assuming LTE and thus a single-temperature LTE model cannot fit the data.
3. There are positions of high C<sub>2</sub>H optical depth in both sources; in addition, L1498 shows self-absorption toward the dust peak.
4. Our Monte Carlo model shows that the observed deviations from LTE can be qualitatively understood, but reliable collisional rate calculations for C<sub>2</sub>H are needed in order to make further progress.
5. The non-LTE deviations have not prevented from computing column density values based on LTE. We also found that the C<sub>2</sub>H abundance relative to H<sub>2</sub> is remarkably constant outside

regions of high CO depletion with a value of  $(1.0 \pm 0.3) \times 10^{-8}$  in L1498 and  $(0.9 \pm 0.3) \times 10^{-8}$  in CB246. One possible implication is that the abundances of atomic oxygen and nitrogen are extremely low (below  $6 \times 10^{-7}$  relative to H).

6. We derived a new set of frequencies for all the six hyperfine components of C<sub>2</sub>H(1–0) and seven components of C<sub>2</sub>H(2–1), computing an improved set of spectroscopic constants for C<sub>2</sub>H.

*Acknowledgements.* This effort/activity is supported by the European Community Framework Programme 7, Advanced Radio Astronomy in Europe, grant agreement no.: 227290. M.P. and D.G. acknowledge support from the EC Research Training Network MRTN-CT-2006-035890 “Constellation: The Origin of Stellar Masses”. H.S.P.M. is grateful for support by the Bundesministerium für Bildung und Forschung (BMBF) administered through Deutsches Zentrum für Luft- und Raumfahrt (DLR). His support is aimed in particular at maintaining the CDMS.

## References

- Aikawa, Y., Ohashi, N. & Herbst, E. 2003, *ApJ*, 593, 906  
Aikawa, Y., Herbst, E., Roberts, H. & Caselli, P. 2005, *ApJ*, 620, 330  
Akyilmaz, M., Flower, D. R., Hily-Blant, P., Pineau Des Forêts, G. & Walmsley, C. M. 2007, *A&A*, 462, 221  
André, P., Ward-Thompson, D. & Motte, F. 1996, *A&A*, 314, 625  
Bel, N. & Leroy, B. 1998 *A&A*, 335, 1025  
Bergin, E. A. & Tafalla, M. 2007, *Ann. Rev. A&A*, 45, 339  
Caselli, P., Myers, P. C. & Thaddeus, P. 1995, *ApJ*, 455, L77  
Caselli, P., Benson, P. J., Myers, P. C. & Tafalla, M. 2002, *ApJ*, 572, 238  
Chandrasekhar, S. & Münch, G. 1950, *ApJ*, 111, 142  
Clemens, D. P. & Barvainis, R. 1988, *ApJS*, 68, 257  
Codella, C. & Scappini, F. 1998, *MNRAS*, 298, 1092  
Crutcher, R. M., Troland, T. H., Lazareff, B. & Kazes, I. 1996, *ApJ*, 456, 217  
Crutcher, R. M. 1999, *ApJ*, 520, 706  
Dame, T. M., Ungerechts, H., Cohen, R. S., de Geus, E. J., Grenier, I. A., May, J., Murphy, D. C., Nyman, L.-A. & Thaddeus, P. 1987, *ApJ*, 322, 706  
Ebenstein, W. L., & Muentner, J. S. 1984, *J. Chem. Phys.*, 80, 3989  
Elias, J. H. 1978, *ApJ*, 224, 857  
Flower, D. R., Pineau Des Forêts, G. & Walmsley, C. M. 2006, *A&A*, 456, 215  
Falgaron, E., Troland, T. H., Crutcher, R. M. & Paubert, G. 2008, *A&A*, 487, 247  
Goodman, A. A., Benson, P. J., Fuller, G. A. & Myers, P. C. 1993, *ApJ*, 406, 528  
Gottlieb, C. A., Gottlieb, E. W. & Thaddeus, P. 1983, *ApJ*, 264, 740  
Green, S. & Thaddeus, P. 1974, *ApJ*, 191, 653  
Guilloteau, S. & Baudry, A. 1981, *A&A*, 97, 213  
Hily-Blant, P., Walmsley, C. M., Pineau des Forêts, G. & Flower, D. 2008, *A&A*, 480, L5  
Hollenbach, D., Kaufman, M. J., Bergin, E. A. & Melnick, G. J. 2009, *ApJ*, 690, 1497  
Kirk, J. M., Ward-Thompson, D. & Crutcher, R. M. 2006, *MNRAS*, 369, 1445  
Launhardt, R. & Henning, T. 1997, *A&A*, 326, 329  
Lee, J.-E., Bergin, E. A. & Evans, N. J. II 2004, *ApJ*, 617, 360  
Lemme, C., Wilson, T. L., Tieftrunk, A. R. & Henkel, C. 1996, *A&A*, 312, 585  
Lique, F., van der Tak, F. F. S., Klos, J., Bulthuis, J. & Alexander, M. H. 2009, *A&A*, 493, 557  
Monteiro, T. S. & Stutzki, J. 1986, *MNRAS*, 221, P33  
Müller, H. S. P., Klaus, T. & Winnewisser, G. 2000, *A&A*, 357, L65  
Müller, H. S. P., Thorwirth, S., Roth, D. A., & Winnewisser, G. 2001, *A&A*, 370, L49-L52  
Müller, H. S. P., Schlöder, F., Stutzki, J., & Winnewisser, G. 2005, *J. Mol. Struct.*, 742, 215  
Myers, P. C., Mardones, D., Tafalla, M., Williams, J. P. & Wilner, D. J. 1996, *ApJ*, 465, L133  
Myers, P. C. & Benson, P. J. 1983, *ApJ*, 266, 309  
Ohashi, N. 1999, in *Proceedings of Star Formation 1999*, ed. T. Nakamoto (Nobeyama Radio Observatory), 129  
Pagani, L., Bacmann, A., Cabrit, S. & Vastel, C. 2007, *A&A*, 467, 179  
Pagani, L., Daniel, F. & Dubernet, M.-L. 2009, *A&A*, 494, 719  
Preibisch, Th., Ossenkopf, V., Yorke, H. W. & Henning, Th. 1993, *A&A*, 279, 577  
Sastry, K. V. L. N., Helminger, P., Charo, A., Herbst, E., & De Lucia, F. C. 1981, *ApJ*, 251, L119  
Schmid-Burgk, J., Muders, D., Müller, H. S. P., & Brupbacher-Gatehouse, B. 2004, *A&A*, 419, 949  
Shinnaga, H., Tsuboi, M. & Kasuga, T. 1999, in *Proceedings of Star Formation 1999*, ed. T. Nakamoto (Nobeyama Radio Observatory), 175  
Shirley, Y. L., Nordhaus, M. K., Greevich, J. M., Evans, N. J., II, Rawlings, J. M. C. & Tatematsu, K. 2005, *ApJ*, 632, 982  
Tafalla, M., Myers, P. C., Caselli, P., Walmsley, C. M. & Comito, C. 2002, *ApJ*, 569, 815  
Tafalla, M., Myers, P. C., Caselli, P. & Walmsley, C. M. 2004, *A&A*, 416, 191  
Tafalla, M., Santiago-García, J., Myers, P. C., Caselli, P., Walmsley, C. M. & Crapsi, A. 2006, *A&A*, 455, 577  
Tassoul, J.-L. 1978, *Theory of Rotating Stars* (Princeton: Princeton Univ. Press)  
Terzieva, R. & Herbst, E. 1998, *ApJ*, 501, 207  
Thum, C., Wiesemeyer, H., Paubert, G., Navarro, S. & Morris, D. 2008, *PASP*, 120, 777  
Turner, B. E., Terzieva, R. & Herbst, E. 1999, *ApJ*, 518, 699  
Walmsley, C. M., Flower, D. R. & Pineau des Forêts, G. 2004, *A&A*, 418, 1035  
Woodall, J., Agúndez, M., Markwick-Kemper, A. J. & Millar, T. J. 2007, *A&A*, 46, 1197